Front. Struct. Civ. Eng. 2025, 19(3): 445–457
https://doi.org/10.1007/s11709-025-1138-y

RESEARCH ARTICLE

The influence of phase change material filled three-dimensional printed artificial aggregates on the properties of blast furnace slag based alkali-activated concrete

Tarik OMUR[a], Ahmet Kaan AKPUNAR[a], Ayşe Betül BINGÖL[b], Büşra OKTAY[b], Cem Bülent ÜSTÜNDAĞ[c], Nihat KABAY[a*]

[a] *Department of Civil Engineering, Yildiz Technical University, Istanbul 34220, Turkey*
[b] *Department of Bioengineering , Yildiz Technical University, Istanbul 34210, Turkey*
[c] *Health Biotechnology Joint Research and Application Center of Excellence, Istanbul 34220, Turkey*
[*] *Corresponding author. E-mail: nkabay@yildiz.edu.tr*

ABSTRACT This study proposes the use of three-dimensional (3D) printed artificial aggregates as phase change material (PCM) carriers and investigates its effects on alkali-activated slag concrete. The artificial aggregates were manufactured using Fused Deposition Modeling (FDM) and Stereolithography (SLA) techniques and PCM was injected into the artificial aggregates. Natural aggregates were replaced with FDM or SLA-type artificial aggregates by 15% and 30% by volume and alkali activated slag concrete specimens were produced. The characteristics of artificial aggregates and their impact on mechanical, physical, and thermal properties of concretes are examined. The results showed that 3D-printed artificial aggregates ameliorated the abrasion resistance of concrete specimens. The concrete samples had a minimum strength of 32 MPa after 28 d, with 15SLA concrete achieving 42.5 MPa, which is comparable to the reference concrete. Thermal test results demonstrated that the PCM helps maintain the concrete surface temperature 3.7 °C higher than the reference mix when the ambient temperature drops below zero and notably slows down the temperature decrease. The concrete mixes without PCM showed ice formation on their surfaces when the ambient temperature dropped to −5 °C, while no ice formation was observed on samples incorporating PCM. Furthermore, the inclusion of PCM improved the freeze–thaw resistance of concretes.

KEYWORDS 3D-printing, artificial aggregate, phase change materials, alkali-activation

1 Introduction

Phase change materials (PCMs) have the ability to store and release thermal energy when they undergo the process of melting and solidifying at particular temperatures [1,2]. PCMs, when added to concrete, can absorb thermal energy as the temperature increases and subsequently release it as the temperature decreases [3,4]. These materials can be incorporated into concrete in a variety of ways, such as impregnating into lightweight aggregates, microencapsulation, macroencapsulation, direct mixing, and porous inclusion techniques [5–8]. However, in order to ensure better performance of PCM in concrete, it is imperative to minimize its leakage and potential interaction with hydration products [9]. The direct mixing, lightweight aggregate and porous inclusion methods could reduce the mechanical performance and may lead to the leakage of PCM [10]. In addition, the low strength, low stiffness, and costly processing are the main drawbacks of the microencapsulation and macroencapsulation techniques [11].

Three-dimensional (3D) printing is a manufacturing technique that allows generating three-dimensional items by adding layers of material on top of each other [12]. 3D

Article history: Received Mar 22, 2024; Accepted Jun 9, 2024

printing has become increasingly popular in recent years because of its capacity to efficiently produce intricate components or prototypes. Fused deposition modeling (FDM) and stereolithography (SLA) rank among the most widely used 3D printing methods. FDM uses a thermoplastic polymer as a filament to construct objects, while SLA uses a liquid resin that is solidified layer-by-layer using ultraviolet (UV) light. There has been an increasing interest in the use of 3D printing technology in the construction sector [13–15] which generally deals with manufacturing concrete blocks in a layered manner using additive manufacturing techniques. In addition, the large scale on-site 3D-printing applications were successfully conducted using natural and recycled aggregate sources [16]. On the other hand, a limited research has also been carried out to manufacture aggregates using the 3D printing methodology. Li et al. [17] utilized 3D printing technology to produce coarse aggregates for asphalt pavements.

The ice formation on concrete surfaces is a prevalent and significant issue due to the harmful impact of deicing agents [18]. The surfaces of concrete bridge decks, viaducts, and pavements are susceptible to the formation of ice and the buildup of snow during severe winter seasons [19]. Employing conventional techniques like deicing salts to address this issue results in significant harm to structures due to reinforcement corrosion and to pavements due to surface scaling, hence reducing their longevity and causing major costs [18,20].

The utilization of PCM in concrete is a remarkable alternative to remove ice and/or snow. Liu et al. [21] found that the incorporation of microencapsulated PCMs effectively inhibits heat diffusion and temperature change in concrete, leading to improved frost resistance and increased freeze–thaw life compared to ordinary concrete. A similar research was conducted by Farnam et al. [22], where they soaked PCM into lightweight aggregate and then incorporated in concrete to investigate their beneficial effects to melt ice and snow.

Alkali-activated materials (AAMs) are environmentally friendly substitutes for ordinary portland cement (OPC) based systems. Their reduced depletion of natural resources, decrease carbon emission, uncomplicated manufacturing process, utilization of waste materials, and versatility make them a preferred eco-friendly construction material [23–26]. In addition, the researches have demonstrated that AAMs, when formulated with the correct mixture designs, exhibit superior mechanical strength, reduced absorption, improved resistance to sulfate and acid, and decreased chloride penetration in comparison to OPC based systems [27–29]. Besides, it was previously reported that alkali-activated slag-based mortars exhibit better resistance to the deicing agent attack compared to the cement-based mortars due to the their minerological compositions [30]. Bukvić and Serdar [31] reported that concretes exposed to sodium chloride salt to prevent ice accumulation was damaged in earlier cycles in alkali-activated concretes, but the severity of damage was lower than the OPC-based concretes.

This study brings together new and sustainable methodologies emerging in today's technology to produce an alternative, cementless composite material with low environmental impact and improved thermal properties. Alkali-activated blast furnace slag-based matrix was utilized to lower the natural resource consumption and environmental impacts, and enhance the durability. The artificial aggregates (AAs) manufactured using two different 3D printing techniques (FDM and SLA) to alleviate the depletion of natural aggregate source. PCM with a low phase transition temperature was injected into the hollow 3D-printed spherical AAs to improve the thermal properties of AAM mixes and prevent or delay the ice formation on the concrete surfaces.

In this scope, 3D-printed AAs were produced with FDM and SLA methods, and the particle strengths of these aggregates were initially determined. Subsequently, the compressive strength, abrasion resistance, freeze–thaw resistance, and thermal properties of alkali-activated slag concretes (AASC) containing various amounts of PCM-injected 3D-printed AAs were investigated.

2 Materials and methodology

2.1 Raw materials

The locally procured ground granulated blast furnace slag (GGBS) with a specific gravity of 2.91 and a blaine fineness of 5420 cm^2/g was used as the binder in AAM preparation. The chemical composition of GGBS based on X-ray fluorescence (XRF) is given in Table 1. Figure 1 displays the X-ray diffraction (XRD) pattern and particle size distribution (PSD) curve of GGBS, obtained using laser particle size analyzer. The raw GGBS shows a highly amorphous structure and a narrow particle size distribution with D_{10}, D_{50}, and D_{90} values of 1.65, 9.93, and 26.2 μm, respectively.

Table 1 The oxide composition of GGBS

Oxides	Content (%)
SiO_2	39.00
Al_2O_3	12.50
Fe_2O_3	1.00
CaO	37.50
MgO	5.00
SO_3	0.20
K_2O	0.20
Na_2O	0.60
Others	4.00

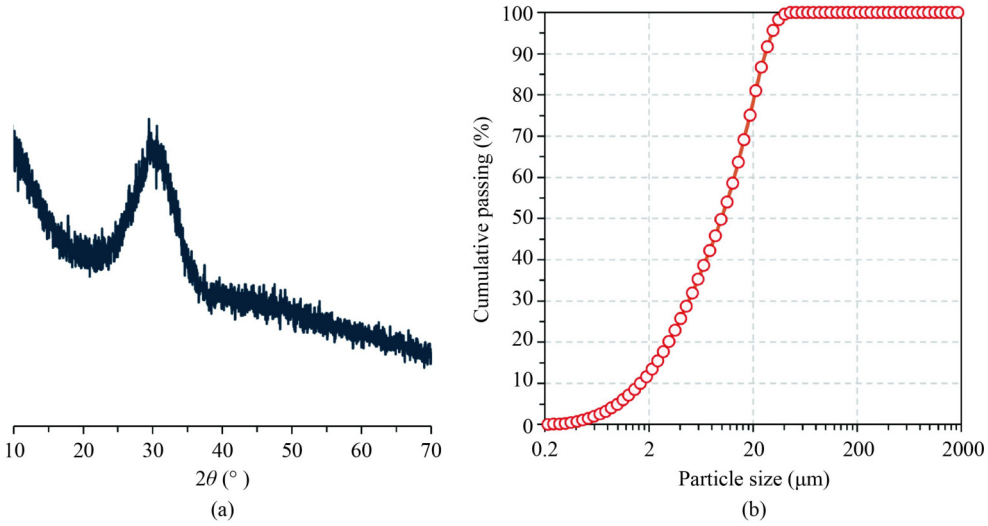

Fig. 1 (a) XRD pattern of GGBS; (b) PSD curve of GGBS.

Fig. 2 From left to right, the appearances of GGBS sand 3D printed FDM aggregates and 3D printed SLA aggregates.

CEN standard sand (particle size ranging between 0.08 and 2 mm) complying with EN 196-1 and siliceous macro-sand with two different particle size ranges of 1–3 mm and 3–6 mm were used as fine and coarse aggregates to produce the AASC mixes. The particle densities of CEN sand and macro-sands were found as 2.67 and 2.68, respectively. In addition, two types of 3D-printed artificial aggregate were used as PCM reservoir and coarse aggregate in AASC samples. The physical appearances of raw materials are depicted in Fig. 2.

A bio-based, nontoxic, biodegradable, and low temperature PCM with a melting point of about 5 °C was used as the temperature regulator in AASC samples. The detailed properties of PCM are tabulated in Table 2. The differential scanning calorimetry (DSC) analysis of PCM is illustrated in Fig. 3. Two distinct peaks were observed during the heating and cooling steps. The endothermic peak indicates the melting point of PCM, which requires 192.4 J/g energy to phase change, while the exothermic peak represents the crystallization of PCM during cooling step, resulting 191.9 J/g energy release. The alkaline solutions were made by combining high purity (> 99%) NaOH granules and a liquid sodium silicate (SS) solution with SiO_2 and Na_2O contents of 27.8% and 8.4%, respectively. The tap water was used to adjust the NaOH molarity and M_s ratio.

Table 2 The physical and thermal properties of PCM

Commercial ID	Melting temperature (°C)	Appearance	Density (kg/m^3)	Bio-based ratio
CrodaTherm 5	~5	liquid/clear	890	94%

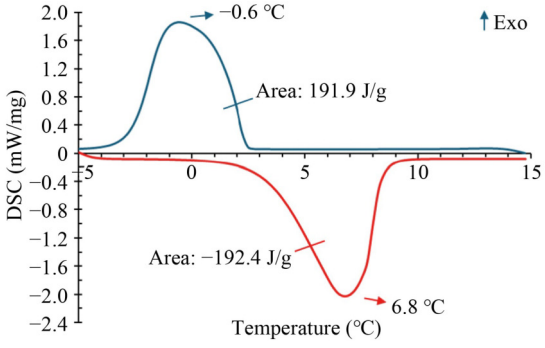

Fig. 3 DSC curve of PCM.

2.2 Manufacture of 3D printed aggregates

The lightweight 3D printed AAs were manufactured via FDM and SLA techniques. Recyclable, natural thermoplastic polyester called polylactic acid (PLA) filament that is derived from renewable resources was used as the main material to produce AAs in FDM method. For SLA method, a UV sensitive clear resin with

a UV wavelength of 405 nm was employed. Figure 4 illustrates the manufacturing stages of AAs using 3D printer. Both methods initially involved creating three-dimensional models of spherical AAs with specific outer diameters and wall thicknesses. These models were then prepared for printing using the freeware slicing softwares of Ultimaker Cura and Chitubox for FDM and SLA methods, respectively. AAs of varying diameters and wall thicknesses were manufactured, and their printability and mechanical properties were examined to identify the optimal sizes for manufacturing. Once the optimal dimensions were determined, the entire internal volume of the AAs was filled with raw PCM prior to incorporation in the mixes.

2.3 Mix design and sample preparation

Table 3 tabulates the mixture proportions of AASC specimens. A total of five concrete mixtures were developed to examine the impact of 3D-printed aggregates on the characteristics of AASC specimens. The natural macro-sands and CEN standard sand were substituted with 3D-printed aggregates by 15% and 30% of the total aggregate volume. Other design parameters such as water-to-binder (w/b) ratio, aggregate-to-concrete volume (a/c) ratio, M_s ratio (SiO_2/Na_2O), and NaOH molarity were maintained constant for each mix. Since the PCM was injected into the 3D-printed AAs, the internal void volume of the spherical AAs was calculated and the percentage of PCM in the total aggregate volume is given in Table 3. The mixtures were coded based on the type and proportion of AAs used. For instance, the '30SLA' signifies that 30% of the aggregate volume in the mixture is composed of AAs manufactured using the SLA method.

The alkaline activator solution was formulated by mixing solid NaOH and liquid SS solution in the appropriate proportions for a duration of 5 min in a glass

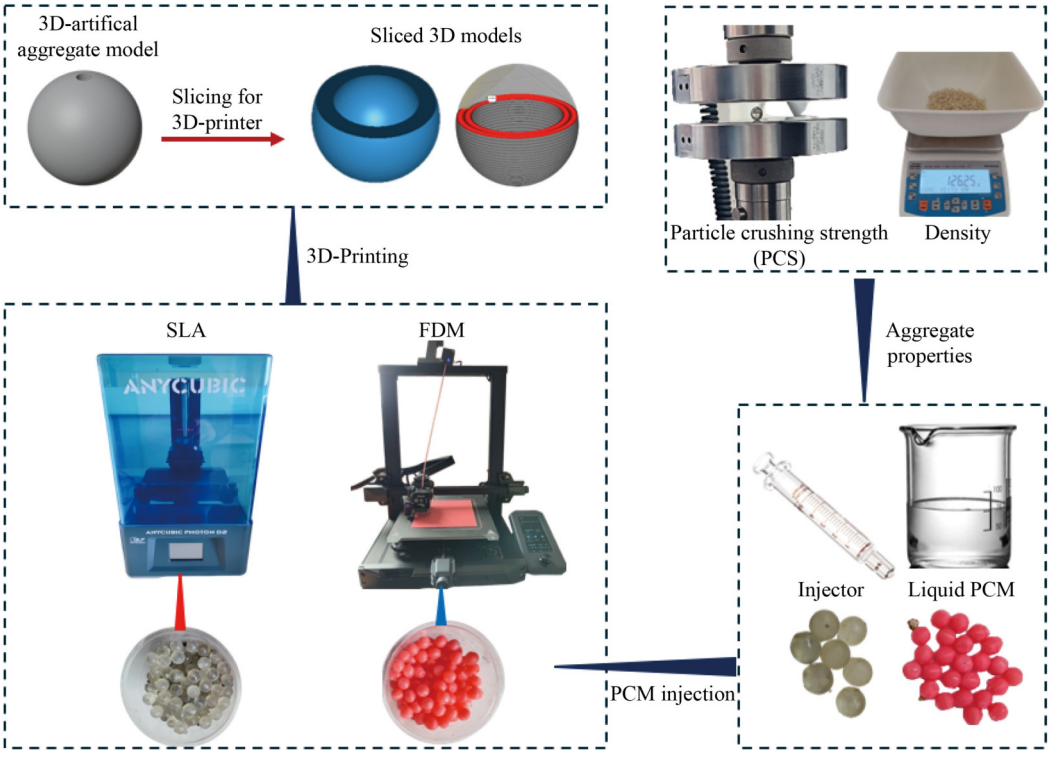

Fig. 4 The schematic demonstration of 3D printed AAs production.

Table 3 The mixture proportions of concrete specimens (g per 1000 cm^3)

Mix ID	GGBS (g)	SS (g)	NaOH (g)	CEN standard sand (g)	Aggregate #1 1-3 mm (g)	Aggregate #2 3-6 mm (g)	SLA AAs (q) [a)]	FDM AAs (q) [a)]	PCM (vol.%)	w/b ratio	a/c ratio [b)] (%)
REF	720.8	211	37.7	667.5	333.8	333.8	–	–	–	0.35	50
15SLA	720.8	211	37.7	567.3	283.5	283.5	280	–	6.3	0.35	50
15FDM	720.8	211	37.7	567.3	283.5	283.5	–	280	6.3	0.35	50
30SLA	720.8	211	37.7	467.2	233.6	233.6	560	–	12.6	0.35	50
30FDM	720.8	211	37.7	467.2	233.6	233.6	–	560	12.6	0.35	50

Notes: a) 'q' represents how many of the relevant AAs are used; b) a/c ratio is given as the ratio of the total aggregate volume to concrete volume.

beaker. The prepared solutions were subsequently sealed and stored in the laboratory for approximately 2 h to cool down to ambient temperature. The production of concrete specimens involved the mixing of the alkaline activator solution, GGBS, natural sand, and/or the AAs in the mixer bowl. The mixing was sustained for 5 min to confirm the uniformity of the mixture. Subsequently, the fresh AASC specimens were transferred into pertinent molds and vibrated for 5 s to expel the air voids. The specimens were removed from their molds after 24 h and stored in a controlled chamber at a temperature and relative humidity of (22 ± 2) °C and 55% ± 2%, respectively.

2.4 Experimental schedule

2.4.1 Aggregate characteristics

The density and particle crushing strength (PCS) tests were performed to characterize the 3D-printed AAs. The density of the AAs was calculated by proportioning the mass and the volume of the spherical aggregates. The stress-strain curves and PCS values of AAs were obtained using an Instron 5982 Electromechanical Universal Testing Machine, as depicted in Fig. 4. The AAs were subjected to vertical load until failure, with a loading rate of 0.5 mm/min. Five aggregate specimens were utilized to ascertain the PCS values for each aggregate type according to Eq. (1).

$$\sigma\,(\mathrm{MPa}) = 2.8 \times \frac{P}{\pi d^2}. \tag{1}$$

In this equation, 'σ' represents the particle crushing strength (MPa), whereas 'P' and 'd' demonstrate the maximum load in N and particle diameter in mm, respectively.

2.4.2 The physical and mechanical tests

The fresh and hardened density of concrete mixes were determined by proportioning the mass and the volume of the specimens, immediately after the production and at 28 d, respectively.

The compressive strength of concrete was determined on 5 cm × 5 cm × 5 cm cubic specimens at 3, 7, and 28 d following ASTM C109 [32] standard.

The Böhme test was employed to evaluate the abrasion resistance of AASC specimens in accordance with EN 1338 [33]. The average weight and length changes were calculated and reported after each abrasion cycle.

The freeze–thaw resistance of AASC mixes was determined following the ASTM C666 [34] standard with a slight modification on the cycle durations. The concrete specimens with dimensions of 7 cm × 7 cm × 7 cm were subjected to freezing at −20 °C followed by thawing at 20 °C. One freeze–thaw cycle was completed in 12 h. The variation of mass and compressive strength was determined after the 150th and 300th cycles. The change in core temperature of the specimens were also recorded using K-type thermocouples during the freeze–thaw test.

2.4.3 Thermal tests

To evaluate the thermal efficiency of PCM-incorporated concretes, two different tests were performed. Figure 5(a) shows a concrete sample with the dimensions of 10 cm × 10 cm × 5 cm before subjected to a thermal cycle to measure the thermal response of concrete surfaces. The sides and the bottom of the AASC specimens were sealed with rock wool to expose only the top surface. The samples were first kept at a temperature of 20 °C for a duration of 24 h. Subsequently, the ambient temperature was gradually reduced to −15 °C within 100 min and the surface temperature of the test samples were recorded every 90 s using a K-type thermocouple.

The experimental setup depicted in Fig. 5(b) was designed to study the effect of PCM on mitigating the ice formation on concrete surfaces in sub-zero environments. Concrete specimens were carefully prepared and wrapped with siliconized glass sheets on all four sides to ensure no

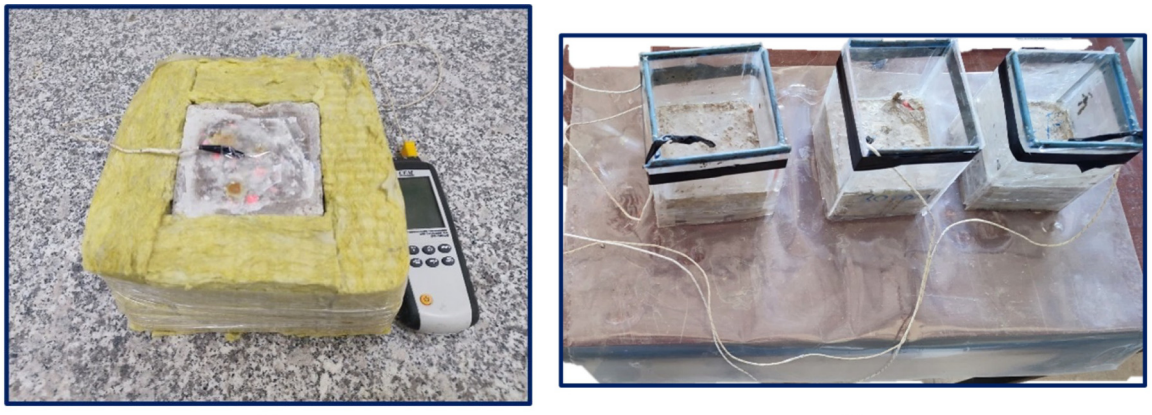

(a) (b)

Fig. 5 (a) The thermal response of concrete surfaces; (b) the observation of ice formation on concrete surfaces.

water leakage. Subsequently, water was added to reach a level of 3 cm higher than the concrete surfaces and thermocouples were carefully positioned to monitor the temperature of water. The ambient temperature was initially set to 20 °C, and gradually decreased to −5 °C. Subsequently, the ambient temperature was increased to 20 °C, and a cycle was completed in 6 h. A total of four consecutive cycles were run and the variation of temperature was recorded simultaneously for each sample.

3 Results and discussion

3.1 Properties of 3D-printed artificial aggregates

Figure 6 illustrates the impact of the external diameter and wall thickness on the mechanical properties of 3D-printed AAs. The AAs were categorized based on their internal and external diameters. As an illustration, the aggregate marked as ‘4−8 mm’ has a 4 mm internal diameter and an 8 mm external diameter. The test results indicated that the AAs printed using the FDM method demonstrate anisotropic characteristics and exhibit varying mechanical properties according to the loading direction. The particle strength of FDM aggregates, when loaded parallel to the filament layers, varied between 2.7 and 3.9 MPa. Conversely, the PCS values ranged from 9.2 to 12.7 MPa, when the AAs are loaded perpendicular to the layers. Furthermore, the strain values of FDM aggregates were reduced by 50% when the load was applied parallel to the layers, compared to that of perpendicular loading. The FDM type of 3D printers construct the model by adding one layer on top of another, starting at the bottom and moving upwards. Consequently, the cohesion between each layer can be compromised when the load is applied in the parallel direction. On the other hand, no variation was detected in the particle strength of SLA type aggregates based on the orientation of the layers. The average results presented in Fig. 6(c) shows that the PCS values of SLA based AAs varied between 8.1 and 13.5 MPa.

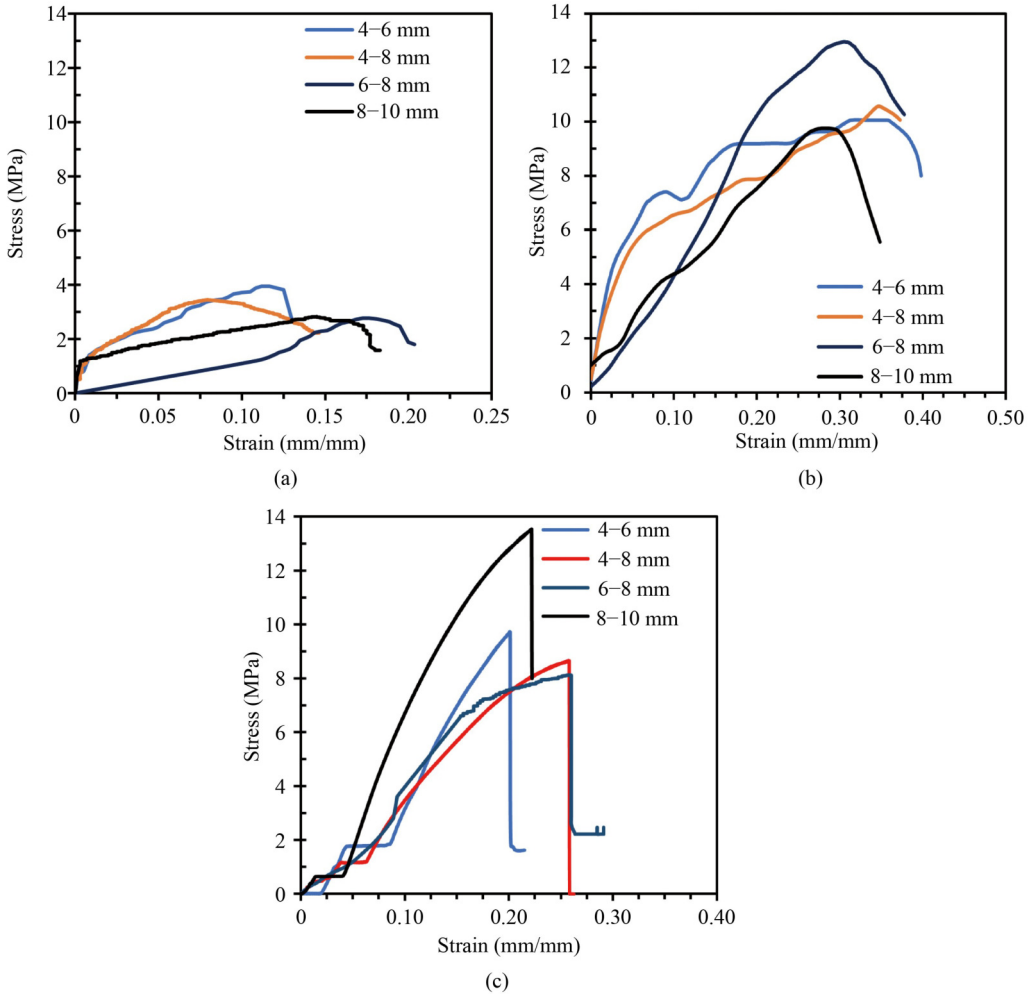

Fig. 6 (a) The stress-strain curves of 3D-printed FDM type AAs (parallel loading); (b) the stress−strain curves of 3D-printed FDM type AAs (perpendicular loading); (c) the stress−strain curves of 3D-printed SLA type AAs.

The change in wall thickness or exterior diameter of FDM type aggregates did not have a substantial impact on the PCS values. Similarly, the increase in the wall thickness of SLA aggregates had little impact on the particle strength. However, in contrast to FDM aggregates, the '8−10' AAs produced with SLA demonstrated the highest PCS value of 13.5 MPa.

The particle density values of PCM-injected AAs with an outer diameter of 8 mm and a wall thickness of 1 mm, produced with FDM and SLA type 3D printers, were determined as 0.93 and 1.35 g/cm^3, respectively, which classifies both of them as lightweight aggregates according to TS EN 1097-6 standard. The variation in the density can be attributed to the printing sensitivity of each method. The FDM technique utilizes a layer thickness of 0.2 mm to print the AAs. On the other hand, the SLA method utilizes UV curing with a layer thickness of 0.05 mm, resulting in a denser material.

3.2 Density and compressive strength

Figure 7 illustrates the fresh and hardened density values of AASC specimens. The fresh density values were in the range of 2063 and 2279 kg/m^3, whereas the hardened density values varied between 1982 and 2209 kg/m^3. The hardened density values were found to be between 2.9% and 5.6% lower than the fresh density values for their corresponding mixtures. This remarkable difference between fresh and hardened density is due to the higher mass loss characteristics of alkali-activated slag mixes. It has been previously reported that AASC samples had higher capillary porosity compared to the conventional cementitious systems, leading to the evaporation of more free water [35], which reduces the hardened density of AASC mixes. The incorporation of AAs consistently reduced both fresh and hardened density values due to their lower particle density compared to natural sand.

The compressive strength development of AASC samples depicted in Fig. 8 shows that the strength of concrete specimens slightly increase from 7 to 28 d reaching 76% to 93% of the 28-d compressive strength values at 7 d. On the other hand, the incorporation of 3D-printed AAs reduced the compressive strength. The

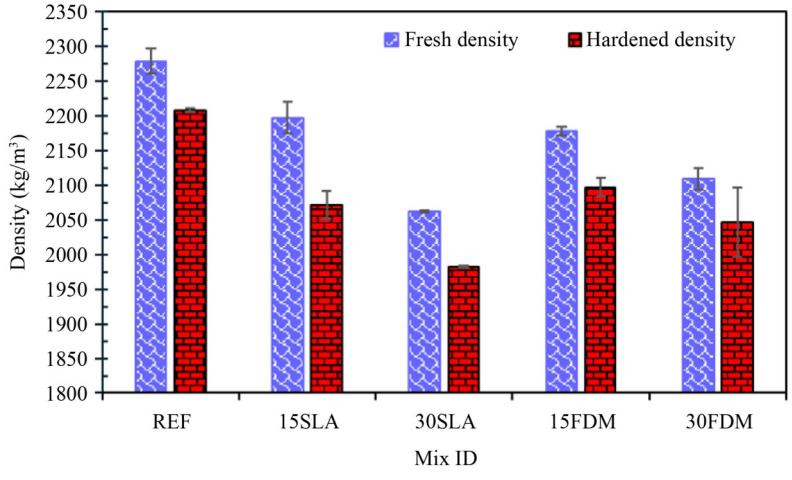

Fig. 7 The fresh and hardened density of AASC.

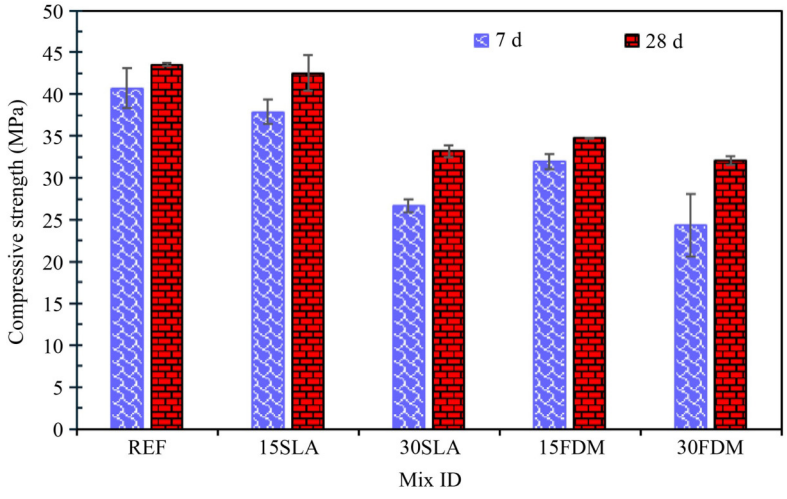

Fig. 8 The compressive strength of AASC.

highest strength recorded was 43.6 MPa in the reference (REF) specimen after 28 d. The inclusion of 15% SLA-based AAs led to a slight reduction in strength achieving 42.5 MPa at 28 d. On the other hand, the concrete containing 30% AAs exhibited a strength reduction of 24% to 26% compared to the REF. The interfacial transition zone (ITZ) between AAM matrix and the AAs surface plays a crucial role in the strength development of concrete mixes [36–39]. The use of 3D-printed AAs with a perfectly circular shape, smooth surface texture, and larger particle size led to an enlargement of the ITZ and a reduction in the bond strength between the matrix and the aggregate surface, resulting in a strength loss. Figure 9 corroborates the existence of a weak bond between the AA and the AASC matrix. The examination of the broken surfaces after the mechanical tests indicated debonding of the 3D-printed AAs from the matrix without breaking and it was determined that the AAs showed low bonding performance compared to natural aggregates. However, the design flexibility of 3D-printing technology can easily overcome this drawback, and the bonding performance of AAs and the strength of ITZ zone may be improved without any extra cost and time. The production of AA with a crushed stone aggregate geometry similar to natural aggregate roughness might lead to an increase in strength by improving the ITZ zone.

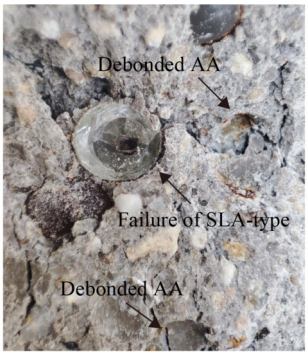

Fig. 9 The appearance of concrete failure surface after the compression test.

The incorporation of SLA-type aggregates in concrete resulted in higher compressive strength values compared to the FDM-type aggregates. The PCS values of AAs play a critical role on the strength of AASC specimens. The anisotropic mechanical properties of FDM-type aggregates may have resulted in the formation of several weak zones within the concrete, resulting in a lower strength compared to mixes incorporating SLA-type AAs.

3.3 Abrasion resistance

Figure 10 displays the change in length and mass of AASC specimens after the abrasion test. After 16 cycles, the specimens experienced a reduction in length ranging from 6.14% to 9.43% and a loss in mass ranging from 7.36% to 11.16%. It was observed that the inclusion of both type of AAs increased the abrasion resistance of concrete by decreasing the length and mass changes. It was found that the reference concrete exhibited a length loss that was 1.52 and 1.54 times more than that of the 30SLA and 30FDM, respectively. Similarly, the reference concrete showed 1.20 and 1.52 times greater mass loss compared to 30SLA and 30FDM, respectively. The improved PCS values, larger particle sizes of AAs, and the reduced contact area between AAs and the abrasion plate due to their ideal circular shape could be the possible factors contributing to the enhanced abrasion resistance of concretes containing AAs. Similarly, prior studies have reported that the utilization of aggregates with coarser particle sizes and harder surfaces enhances the abrasion resistance of concrete [40,41].

3.4 Thermal properties

Figure 11 depicts the development of the surface temperatures of concrete samples with elapsed time. The test results indicated a clear disparity between the

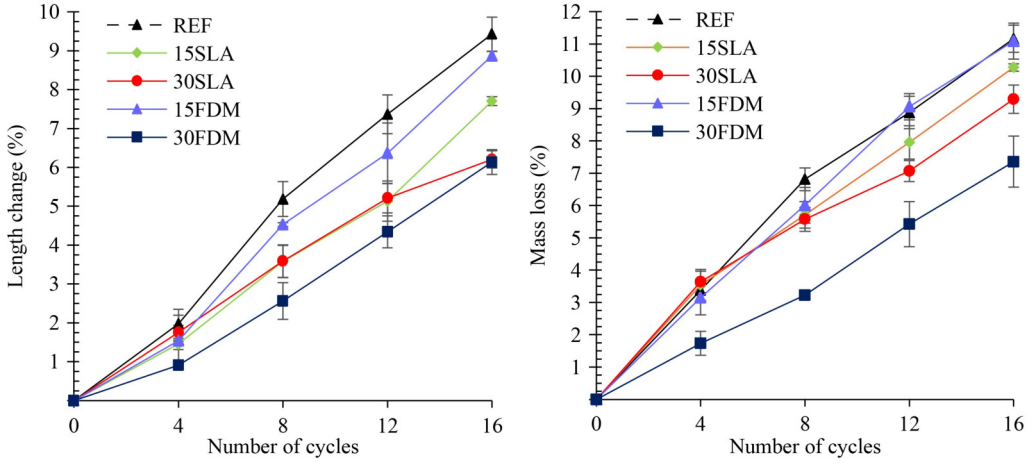

Fig. 10 Böhme test results of AASC mixes.

reference and the PCM-incorporated concretes. As the ambient temperature was gradually reduced to −20 °C, the surface temperature curve of reference concrete showed a sharper reduction, whereas the decrease in the surface temperature of the mixtures containing PCM-injected aggregates was remarkably delayed. Furthermore, the incorporation of PCM containing AAs ensures the surface temperatures of the concrete remain significantly higher than the ambient temperature for an extended period during the phase transition range of the PCM. For instance, the incorporation of PCM resulted in a delay of approximately 40 to 60 min for the concrete surface temperature to drop below 0 °C, compared to the reference. Moreover, the surface temperature of PCM incorporated mixes were found to remain up to 3.7 °C higher than the reference sample under sub-zero conditions. This improved thermal performance is due to the PCM. PCMs function by undergoing a phase transition between solid and liquid states, during which they absorb and release thermal energy [9] and help maintain the temperature around their phase transition temperature. As shown in Fig. 11, the temperature delaying effect started around 5 °C, which is the melting point of the PCM.

Both FDM and SLA type AAs exhibited comparable thermal performance in the AASC samples with slight variations, which is possibly due to the different thermal conductivity values of the raw materials used to construct the AAs. Moreover, the increase in the AAs content and accordingly the PCM content in concrete enhanced the thermal efficiency, regardless of the AAs type.

Figure 12 shows the impact of PCM-injected 3D-

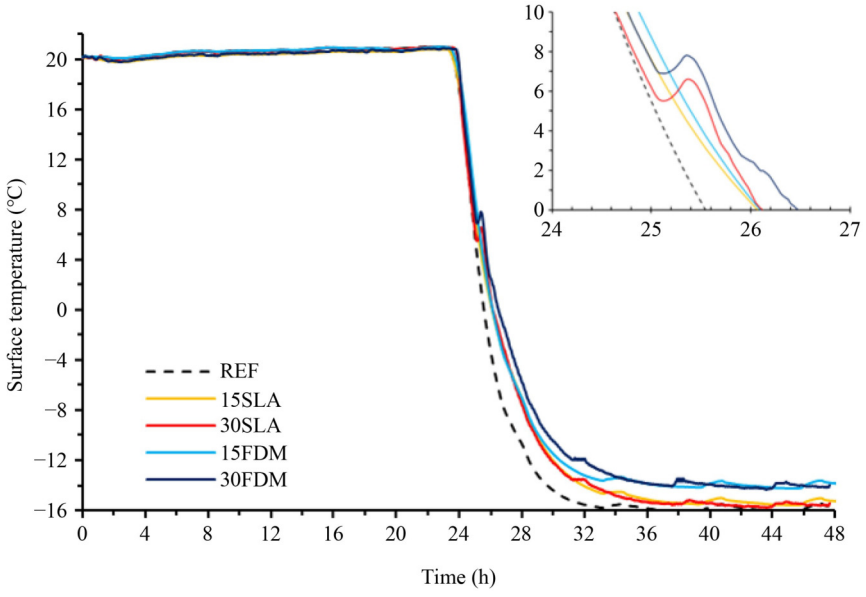

Fig. 11 The effect of PCM inclusion on the thermal response of concrete surfaces.

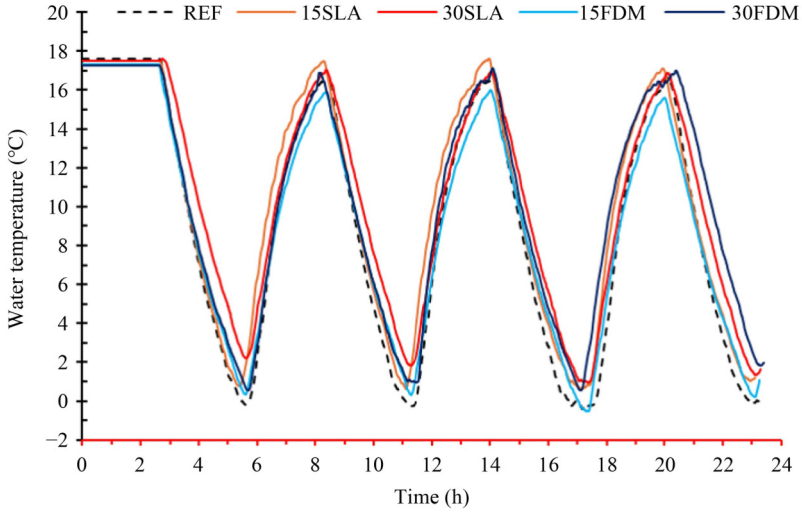

Fig. 12 The development of water/ice temperature on the concrete surface.

printed aggregates on delaying the ice formation over the concrete surfaces. The ambient temperature was gradually decreased to −5 °C to simulate the typical winter circumstances, and the water temperature was monitored for four cycles. The test results indicated that the water layer temperature over the reference concrete dropped below 0 °C in all four cycles leading to ice formations, whereas the water layer on the surface of the PCM-containing concretes mostly showed no sign of freezing. The water layer temperature of the 30SLA and 30FDM concrete samples exhibited higher values, up to 1.9 and 2.1 °C, respectively, compared to the reference, which protected the transformation of water into ice. The results also showed that the aggregate type had negligible effect on the deicing performance. On the other hand, the quantity of AAs and eventually PCM content had a direct influence as the higher PCM-injected AAs ratio in concrete helped to achieve higher water temperature values.

3.5 Freeze–thaw resistance

The freeze–thaw resistance of concrete samples was determined by measuring the residual compressive strength and by monitoring the core temperature of the concrete samples up to 150 and 300 cycles. Figure 13 illustrates the residual compressive strength results of concrete specimens. The compressive strength of all investigated samples decreased after the freeze–thaw cycles. However, it is noteworthy that all AASC specimens maintained their structural integrity even after 300 cycles, and no significant mass loss or scaling was observed. These observations reveal that the alkali-activated GGBS concrete shows superior durability against freeze–thaw effects. Similarly, it has been reported that the formation of reaction products such as hydrotalcite and tetrazine zeolite in AASC create a dense microstructure that decreases the porosity and limits water penetration, resulting in improved resistance to freeze–thaw cycles compared to the conventional OPC-based systems [42]. The residual compressive strength values of concrete specimens after 150 and 300 cycles varied in the range between 88.5%–99.5% and 86.6%–94.3%, respectively. Incorporating PCM-containing AAs improved the resistance to freeze–thaw cycles. For instance, only 0.5% and 5.7% strength loss was observed in 30SLA after 150 and 300 freeze–thaw cycles, respectively. The results also suggest that the concrete samples containing SLA-type AAs show slightly higher residual compressive strength values compared to FDM-type AAs after the freeze–thaw cycles. In addition, the increase in AAs content led to higher residual strength values, irrespective of the AAs type.

Figure 14 depicts the core temperatures of AASC samples before and after the freeze–thaw cycles. Regardless of the type and amount of AAs used, the addition of PCM slightly improved the core temperatures of the mixtures compared to the reference concrete.

The application of PCM in concrete faces challenges such as the chemical interaction of PCM with concrete, degradation of encapsulation material, and leaking of liquid PCM [1,43]. Besides, an essential concern is ensuring that the heat storage feature of the PCM remains functional during repeated use [8,44]. Multiple cycles of melting and solidification might cause performance loss in the thermal storage capability of the PCM, which is crucial for their efficient utilization in concrete. As shown in Figs. 13 and 14, the PCM continued to function well after 150 and 300 freeze–thaw cycles. Figure 15 demonstrates the absence of any PCM leakage issue during the freeze–thaw cycles. After the compression test following 300th freeze–thaw cycle, PCM leakage is observed through the broken AA particle during the compression test which shows that the PCM remains stable in the AA.

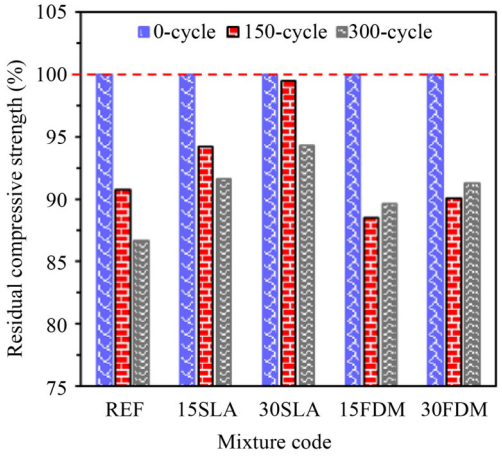

Fig. 13 The residual compressive strength of AASC samples after freeze–thaw cycles.

4 Conclusions

This study proposed the utilization of FDM and SLA type 3D-printed AAs containing PCM as an alternative aggregate source and thermoregulator material in alkali-activated GGBS-based concretes. Lightweight 3D-printed AAs with hollow spherical shape were successfully manufactured via FDM and SLA-type 3D-printers using PLA and UV sensitive resin as the raw materials, respectively. The raw PCM was injected into the AAs and then incorporated into the concrete at varying ratios. The characteristics of PCM-containing 3D-printed aggregates and their effects on the mechanical, physical and thermal properties of AASC specimens are discussed. The following conclusions can be drawn from the experimental studies.

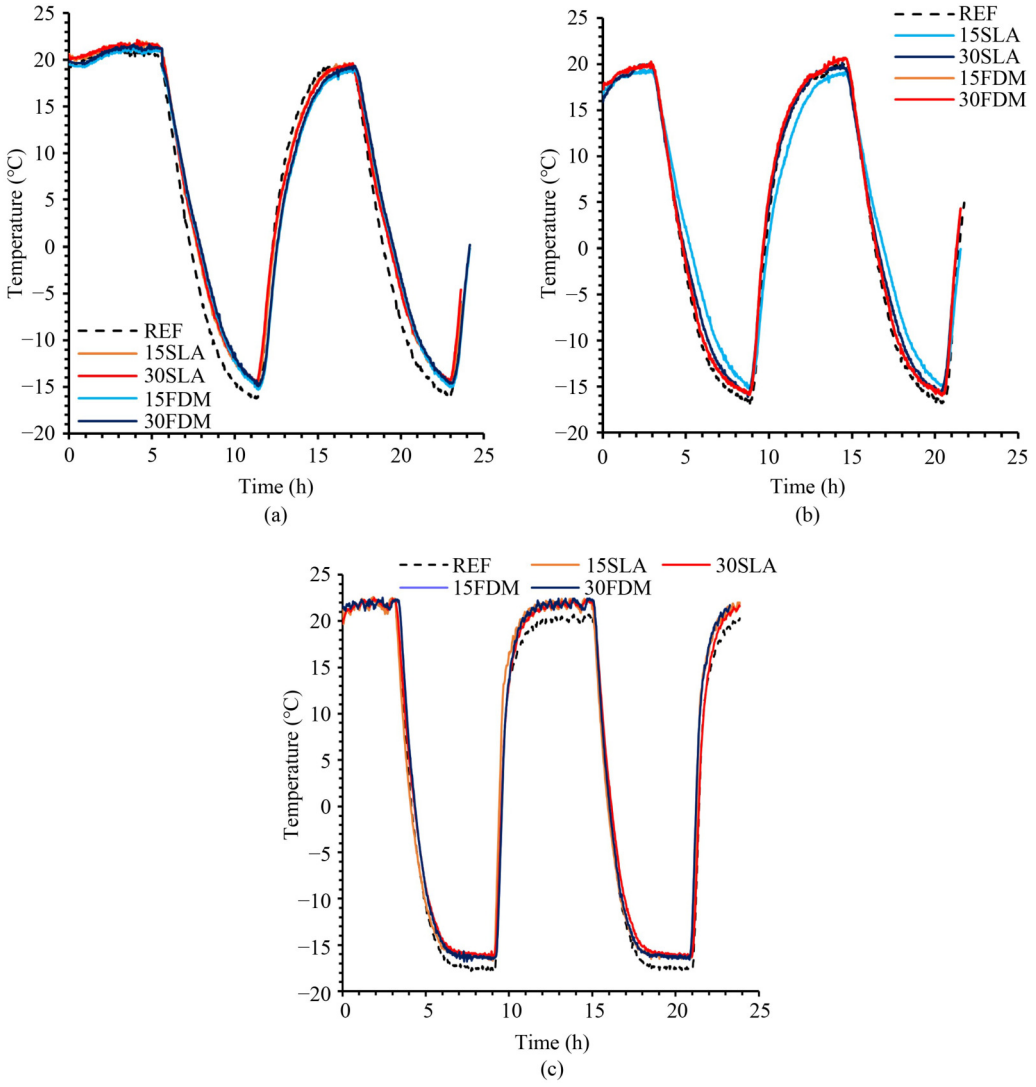

Fig. 14 (a) Thermal responses of AASC specimens before freeze–thaw cycles; (b) thermal responses of AASC specimens after subjected to 150th freeze–thaw cycles; (c) thermal responses of AASC specimens after subjected to 300th freeze–thaw cycles.

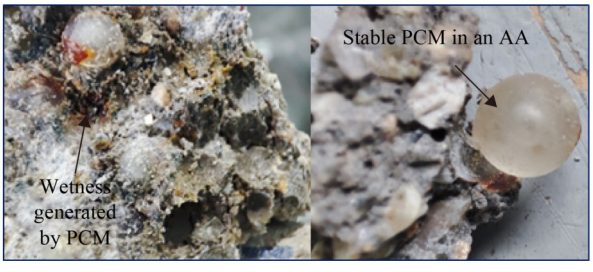

Fig. 15 The appearance of AASC samples after the compression test following 300th freeze–thaw cycle.

1) The FDM-type AAs exhibited anisotropic characteristics and varying mechanical properties according to the loading direction. On the other hand, no variation was detected in the particle strength of SLA-type aggregates based on the orientation of the layers and the PCS values ranged from 8.1 to 13.5 MPa.

2) The inclusion of both FDM or SLA-type AAs consistently reduced the compressive strength of AASC specimens due to the weak bonding between the spherical AAs and the AASC matrix. On the other hand, the abrasion resistance of AASC samples was significantly ameliorated with the incorporation of both FDM and SLA type AAs.

3) Thermal tests revealed that incorporating AAs with PCM can keep the surface temperature of concrete up to 3.7 °C warmer and can delay the onset of sub-zero temperatures by up to 1 h, compared to the reference concrete.

4) The addition of PCM-containing AAs into AASC efficiently prevented the ice formation on the concrete surface when the ambient temperature was reduced to –5 °C. Another positive effect of PCM-filled AAs on the thermal behavior was improved freeze–thaw resistance of AASC specimens after 150 and 300 cycles. The concretes with PCM containing AAs had higher residual compressive strength values compared to the reference

concrete, improving the resistance against freeze and thawing effects.

5) Overall, the use of PCM-injected AAs manufactured by FDM or SLA type 3D-printing technique in concrete improved the abrasion resistance, thermal properties, and prevented ice formation on the concrete surface without any sign of PCM leakage.

Acknowledgements The second author would like to acknowledge that this paper is submitted in partial fulfillment of the requirements for a Ph.D. degree at Yildiz Technical University. This work has been supported by Yildiz Technical University Scientific Research Projects Coordination Unit under project number FDK-2022-4808.

Competing interests The authors declare that they have no conflict of interest.

References

1. Adesina A. Use of phase change materials in concrete: Current challenges. Renewable Energy and Environmental Sustainability, 2019, 4: 9
2. Hao L, Xiao J, Cao W, Sun J. Experimental study and assessment of thermal energy storage mortar with paraffin/recycled brick powder composite phase change materials. Frontiers of Structural and Civil Engineering, 2022, 16(10): 1301–1314
3. Asadi I, Jacobsen S, Baghban M H, Maghfouri M, Hashemi M. Reviewing the potential of phase change materials in concrete pavements for anti-freezing capabilities and urban heat island mitigation. Buildings, 2023, 13(12): 3072
4. Rashid F L, Al-Obaidi M A, Dulaimi A, Bernardo L F A, Eleiwi M A, Mahood H B, Hashim A. A review of recent improvements, developments, effects, and challenges on using phase-change materials in concrete for thermal energy storage and release. Journal of Composites Science, 2023, 7(9): 352
5. Liu F, Wang J, Qian X. Integrating phase change materials into concrete through microencapsulation using cenospheres. Cement and Concrete Composites, 2017, 80: 317–325
6. Rathore P K S, Shukla S K. Potential of macroencapsulated PCM for thermal energy storage in buildings: A comprehensive review. Construction and Building Materials, 2019, 225: 723–744
7. Ling T C, Poon C S. Use of phase change materials for thermal energy storage in concrete: An overview. Construction & Building Materials, 2013, 46: 55–62
8. Sharma R, Jang J G, Hu J W. Phase-change materials in concrete: Opportunities and challenges for sustainable construction and building materials. Materials, 2022, 15(1): 335
9. Salunkhe P B, Shembekar P S. A review on effect of phase change material encapsulation on the thermal performance of a system. Renewable & Sustainable Energy Reviews, 2012, 16(8): 5603–5616
10. Li H, Chen H, Li X, Sanjayan J G. Development of thermal energy storage composites and prevention of PCM leakage. Applied Energy, 2014, 135: 225–233
11. Konuklu Y, Ostry M, Paksoy H O, Charvat P. Review on using microencapsulated phase change materials (PCM) in building applications. Energy and Building, 2015, 106: 134–155
12. Zukas V, Zukas J A. An Introduction to 3D Printing. Sarasota, FL: First Edition Design Pub., 2015
13. Sanjayan J G, Nazari A, Nematollahi B. 3D Concrete Printing Technology: Construction and Building Applications. Oxford: Butterworth-Heinemann, 2019
14. Hossain M A, Zhumabekova A, Paul S C, Kim J R. A review of 3D printing in construction and its impact on the labor market. Sustainability, 2020, 12(20): 8492
15. Schuldt S J, Jagoda J A, Hoisington A J, Delorit J D. A systematic review and analysis of the viability of 3D-printed construction in remote environments. Automation in Construction, 2021, 125: 103642
16. Xiao J, Zou S, Yu Y, Wang Y, Ding T, Zhu Y, Yu J, Li S, Duan Z, Wu Y, Li L. 3D recycled mortar printing: System development, process design, material properties and on-site printing. Journal of Building Engineering, 2020, 32: 101779
17. Li W, Wang D, Chen B, Hua K, Huang Z, Xiong C, Yu H. Preparation of artificial pavement coarse aggregate using 3D printing technology. Materials, 2022, 15(4): 1575
18. Sanchez T, Conciatori D, Keserle G C. Influence of the type of the de-icing salt on its diffusion properties in cementitious materials at different temperatures. Cement and Concrete Composites, 2022, 128: 104439
19. Yessentay D E, Kiyalbaev A K, Kiyalbay S N, Borisyuk N V. Substantiation of application of anti-ice chemical reagents on automobile roads with cement concrete covering. News of the NAS RK. Chemistry and Technology Series, 2021, 1(445): 112–118
20. Chen X, Gao P. Experimental study on salt freezing damage of cement concrete by chloride deicing agent. In: Proceedings of IOP Conference Series: Earth Environtal Science. Bristol: IOP Publishing, 2021: p. 022070
21. Liu F, Tang R, Ma W, Yuan X. Frost resistance and meso-deterioration analysis of microcapsulated phase change materials modified concrete. Journal of Building Engineering, 2022, 61: 105214
22. Farnam Y, Krafcik M, Liston L, Washington T, Erk K, Tao B, Weiss J. Evaluating the use of phase change materials in concrete pavement to melt ice and snow. Journal of Materials in Civil Engineering, 2016, 28(4): 04015161
23. Glanz D, Sameer H, Göbel D, Wetzel A, Middendorf B, Mostert C, Bringezu S. Comparative environmental footprint analysis of ultra-high-performance concrete using Portland cement and alkali-activated materials. Frontiers in Built Environment, 2023, 9: 1196246
24. He J, Yu S, Sang G, He J, Wang J, Chen Z. Properties of alkali-activated slag cement activated by weakly alkaline activator. Materials, 2023, 16(10): 3871
25. Lanjewar B A, Chippagiri R, Dakwale V A, Ralegaonkar R V. Application of alkali-activated sustainable materials: A step towards net zero binder. Energies, 2023, 16(2): 969
26. Singh J, Singh S P. Utilization of alkali-activated copper slag as binder in concrete. Frontiers of Structural and Civil Engineering, 2021, 15(3): 773–780

27. M L K, Revathi V. Durability studies in alkaline activated systems (metakaolin-bottom ash): A prospective study. Journal of the Spanish Ceramic and Glass Society, 2023, 62(1): 40–55
28. Thenmozhi R, Vijaya Prabha C. A study of alkali-activated coatings durability assessment in different environments. Polish Journal of Environmental Studies, 2023, 32(4): 3323
29. Mohamed O A, Al-Khattab R, Al-Hawat W. Resistance to acid degradation, sorptivity, and setting time of geopolymer mortars. Frontiers of Structural and Civil Engineering, 2022, 16(6): 781–791
30. Coffetti D, Cabrini M, Crotti E, Gazzaniga G, Lorenzi S, Pastore T, Coppola L. Durability of mortars manufactured with low-carbon binders exposed to calcium chloride-based de-icing salts. Key Engineering Materials, 2022, 919: 151–160
31. Bukvić O, Serdar M. Freeze–thaw resistance with de-icing salts of alkali-activated slag concrete: The influence of activator type and dosage and comparison to the ordinary Portland cement concrete. In: Proceedings of 8th Symposium on Doctoral Studies in Civil Engineering. Zagreb: University of Zagreb Faculty of Civil Engineering, 2022, 213–224
32. ASTM. Standard Test Method for Compressive Strength of Hydraulic Cement Mortars (Using 50 mm Cube Specimens), ASTM C109/C109M-21. West Conshohocken, PA: ASTM, 2010
33. EN-1338. Concrete paving blocks—Requirements and Test Methods. Brussels: European Committee for Standardization, 2003
34. ASTM. Standard Test Method for Resistance of Concrete to Rapid Freezing and Thawing. ASTM C666/C666M-03. West Conshohocken, PA: ASTM, 2003
35. Li Z, Lu T, Liang X, Dong H, Ye G. Mechanisms of autogenous shrinkage of alkali-activated slag and fly ash pastes. Cement and Concrete Research, 2020, 135: 106107
36. Almadani M, Razak R A, Abdullah M M A B, Mohamed R. Geopolymer-based artificial aggregates: A review on methods of producing, properties, and improving techniques. Materials, 2022, 15(16): 5516
37. Zou S, Chau C K, Leung L M, Duan Z, Xiao J, Sham M L, Poon C S. Developing low-carbon high-strength core-shell aggregates using solid waste by cold-bonding techniques. Construction & Building Materials, 2024, 416: 135116
38. Xiao J. Springer Tracts in Civil Engineering Recycled Aggregate Concrete Structures. Berlin: Springer-Verlag GmbH, 2018
39. Tang Y, Xiao J, Zhang H, Duan Z, Xia B. Mechanical properties and uniaxial compressive stress–strain behavior of fully recycled aggregate concrete. Construction and Building Materials, 2022, 323: 126546
40. Al-Akhaly İ. Engineering properties of basalt coarse aggregates in Hamdan Area, NW Sana'a, Yemen. Journal of Geological Engineering, 2018, 42(2): 159–174
41. Toklu K, YAZICIOĞLU S. The Effect of aggregate size and cure conditions on the engineering properties of concrete. Turkish Journal of Science and Technology, 2020, 15: 127–137
42. Chen B, Wang J. Experimental study on the durability of alkali-activated slag concrete after freeze–thaw cycle. Advances in Materials Science and Engineering, 2021, 2021: 1–19
43. Heniegal A M, Ibrahim O M O, Frahat N B, Amin M. Thermal and mechanical properties of mortar incorporated with phase change materials (PCMs). Key Engineering Materials, 2022, 921: 259–269
44. Çelik A İ, Kayabaşi R, Şener A. A literature review about effects of phase changing material on compressive strength and thermal conductivity of building components. Engineering Sciences and Design Journal, 2022, 10(4): 1495–1508